Journal of Materials Research and Technology 42 (2026) 5192–5199

Contents lists available at ScienceDirect

Journal of Materials Research and Technology

journal homepage: www.elsevier.com/locate/jmrt

Flexible PEDOT:PSS thermoelectrics reinforced by HESO8@Sb2Te3 core–shell networks

Jinhyun Park [a], Oju Kwon [a], Sangwoo Kim [a], Nahyun Lee [a], Dabin Park [c], Jooheon Kim [a,b,*]

[a] School of Chemical Engineering, Chung-Ang University, Seoul, 06974, Republic of Korea
[b] Department of Intelligent Energy and Industry, Graduate School, Chung-Ang University, Seoul, 06974, Republic of Korea
[c] Department of Mechanical and Aerospace Engineering, University of California, Irvine, CA, 92679, USA

ARTICLE INFO

Keywords:
Thermoelectric composites
PEDOT:PSS
Sb_2Te_3
Core–shell fillers

ABSTRACT

Flexible polymer thermoelectrics were realized by dispersing core–shell HESO8@Sb_2Te_3 particulates within a PEG-assisted PEDOT:PSS matrix. Leveraging the high-entropy spinel (HESO8) core for mass-fluctuation/point-defect phonon scattering, the composites suppress thermal conductivity (κ), while the Sb_2Te_3 shell contributes to interfacial carrier-transport modulation and percolation-aided charge transport across the conducting network. Solution processing yielded self-supporting films with filler contents of 5–20 wt%. Among them, the 10 wt% specimen provided the most balanced response throughout 300–475 K, exhibiting a monotonic rise in Seebeck coefficient with temperature and a peak conductivity near 425 K. At ~425 K, the film delivered ZT ≈ 0.50 with κ ≈ 0.21 W m^{-1} K^{-1} and PF ≈ 2.4 × 10^2 μW m^{-1} K^{-2}. The performance stems from the dual action of (i) κ reduction via the spinel core and abundant polymer–filler interfaces and (ii) PF enhancement associated with Sb_2Te_3-mediated interfacial carrier transport together with PEG-induced PEDOT-rich pathways. This spinel–telluride core–shell strategy offers a scalable route to low-κ, high-PF polymer thermoelectrics operating from room to mid-temperature.

1. Introduction

Recovering low-grade heat as electricity is increasingly vital for sustainable energy systems. Thermoelectric (TE) technology enables direct heat–to–electric conversion in solid-state devices, offering compactness, zero local emissions, and high reliability—attributes attractive for energy harvesting from distributed low-temperature sources such as industrial equipment, data centers, electronics, and wearables [1–4]. In practice, meaningful efficiency gains originate at the materials level: device or system design cannot compensate for limitations in intrinsic charge- and heat-transport properties. Consequently, TE materials are often deemed "promising yet still short of commercial efficiency," a judgment rooted in their transport constraints [5,6]. For research, development, and fair comparison, performance is consistently expressed by two material metrics:

$$PF = S^2\sigma \tag{1}$$

$$ZT = \frac{S^2\sigma T}{\kappa}, \kappa = \kappa_L + \kappa_e \tag{2}$$

where S is the Seebeck coefficient, σ the electrical conductivity, κ the total thermal conductivity comprising lattice (κ_L) and electronic (κ_e) parts, and T the absolute temperature [7–9]. Maximizing ZT ideally requires large S, high σ, and low κ at once, yet these quantities are mutually entangled: increases in σ typically raise κ_e via the Wiedemann–Franz relation, while S anticorrelates with carrier concentration (Pisarenko trend), creating tension with σ. Lowering κ—dominated by κ_L—by introducing more grain boundaries, defects, or interfaces strengthens phonon scattering but may degrade mobility μ and thus σ. The design imperative is therefore a selective partition of transport: retain continuous electronic pathways while suppressing lattice heat conduction [10–14].

At near-room temperature, Sb_2Te_3-based p-type chalcogenides serve as representative benchmarks owing to their high carrier mobility and favorable electronic transport characteristics. However, their intrinsically high crystallinity leads to a long phonon mean free path, making it difficult to suppress lattice thermal conductivity (κ) without concurrently compromising electrical conductivity (σ). This inherent σ–κ trade-off limits further improvement of the thermoelectric figure of merit,

* Corresponding author. School of Chemical Engineering, Chung-Ang University, Seoul, 06974, Republic of Korea.
E-mail address: jooheonkim@cau.ac.kr (J. Kim).

https://doi.org/10.1016/j.jmrt.2026.04.128
Received 30 December 2025; Received in revised form 5 April 2026; Accepted 15 April 2026
Available online 18 April 2026
2238-7854/© 2026 The Authors. Published by Elsevier B.V. This is an open access article under the CC BY license (http://creativecommons.org/licenses/by/4.0/).

particularly under conditions where phonon scattering must be intensified. In parallel, oxide thermoelectrics such as spinel-type high-entropy oxides exhibit intrinsically strong phonon scattering arising from mass and elastic disorder, resulting in inherently low κ together with excellent thermal and chemical stability. Yet their localized electronic states typically yield low σ, constraining the achievable power factor despite moderate or high Seebeck coefficients. To complement these inorganic systems, conductive polymers such as PEDOT:PSS provide intrinsically low κ, mechanical flexibility, and solution processability, making them attractive matrix candidates for flexible and large-area devices [15–18]. However, their electrical conductivity and long-term stability still lag behind those of inorganic chalcogenides, so that polymers alone cannot meet the requirements for high-performance thermoelectrics. Bridging these contrasting profiles—high-σ but κ-limited Sb_2Te_3-based chalcogenides, low-κ but σ-deficient oxides, and flexible yet moderately conducting polymers—has motivated extensive efforts in nanostructuring, hierarchical interfaces, core–shell heterostructures, and organic–inorganic hybrids. Nevertheless, many of these systems continue to suffer from interface-limited carrier transmission, shell discontinuity, aggregation-induced mobility loss, and scale-up challenges within polymer matrices [19–21].

In particular, PEDOT:PSS/Sb_2Te_3 composites have demonstrated the utility of Sb_2Te_3 for improving thermoelectric transport in flexible polymer-based systems. At the same time, further expanding the role of the inorganic filler toward more effective suppression of lattice heat transport remains an important design opportunity. In this context, the incorporation of a high-entropy oxide component offers an additional structural route to intensify phonon scattering while retaining the established thermoelectric advantages of Sb_2Te_3-based phases. This provides the basis for exploring composite architectures in which charge transport and lattice heat transport can be more effectively balanced within PEDOT:PSS-based thermoelectrics.

Motivated by this design opportunity, this work employs a core–shell/polymer hybrid comprising high-entropy spinel oxide (HESO8) cores wrapped by Sb_2Te_3 shells and dispersed in PEG/methanol-treated PEDOT:PSS. The design aligns with Eqs. (1) and (2) through three complementary elements. (i) The HESO8 core, characterized by mass/elastic disorder and local strain fields, is expected to suppress κL by promoting phonon scattering. [22–27]. (ii) A continuous Sb_2Te_3 shell network preserves p-type pathways and sustains σ, while the aligned molecular structure of the PEG/methanol-treated PEDOT:PSS matrix contributes to electronic percolation [28–30]. (iii) The multiphase interfaces among core, shell, and polymer add thermal boundary resistance, further suppressing lattice heat transport [9,31,32]. Overall, the architecture is designed to combine the favorable p-type transport characteristics of Sb_2Te_3 with the enhanced phonon-scattering potential of the HESO8 core in a solution-compatible PEDOT:PSS platform, with the aim of lowering κ while maintaining a practical PF.

2. Results and discussion

The stepwise fabrication process of the HESO8@Sb_2Te_3/PEDOT:PSS-PEG composites is outlined in Fig. 1.

2.1. Characterization of HESO8

HESO8 nanoparticles (NPs) with the composition $(Co, Mg, Mn, Ni, Zn)(Al, Co, Cr, Fe, Mn)_2O_4$ were synthesized. Electron microscopy reveals particle diameters in the range of approximately 50–100 nm (Fig. 2a), while EDS mapping confirms spatially uniform distributions of Mg, Mn, Co, Ni, Zn, Al, Cr, Fe, and O across the particles (Fig. 2b). The XRD pattern is indexed to a single spinel phase (Fd-3m), with no secondary reflections detectable within instrumental limits (Fig. 2c). To further verify the elemental composition of HESO8, ICP-AES analysis was additionally conducted (Table S1). The measured elemental contents were Mg 1.62 wt%, Mn 14.92 wt%, Ni 5.65 wt%, Co 17.52 wt%, Cr 9.58 wt%, Al 3.20 wt%, Fe 10.26 wt%, and Zn 5.93 wt%. Because ICP-AES quantifies only the metallic elements, oxygen was not included in the reported composition. These results, together with the observed particle size, compositional homogeneity, and diffraction pattern, are consistent with literature reports of high-entropy spinels [22], validating HESO8 as a suitable precursor for subsequent core–shell synthesis and composite fabrication.

2.2. Characterization of HESO8@Sb_2Te_3

TEM reveals discrete HESO8@Sb_2Te_3 particles in which a ~100–200 nm HESO8 core is surrounded by a lighter-contrast Sb_2Te_3 shell, evidencing a clear core–shell contrast (Fig. 3a). STEM–EDS elemental maps corroborate this architecture: Sb and Te are distributed across the entire particle, while the core-forming elements (Mg, Mn, Co, Ni, Zn, Al, Cr, Fe) together with O are enriched in the interior core region (Fig. 3b). The XRD pattern indexes to rhombohedral Sb_2Te_3 (R-3m) and shows no detectable impurity reflections within instrumental limits, in agreement with the Sb_2Te_3 reference pattern (PDF #15-0874) (Fig. 3c). The absence of discernible spinel reflections is attributed to the dominant diffraction of the shell and/or the limited scattering volume of the buried core. Collectively, TEM/EDS/XRD unambiguously confirm the successful formation of an Sb_2Te_3 shell and a chemically uniform core–shell structure suitable for subsequent thermoelectric measurements. The Sb_2Te_3 shell thickness was further quantified from the TEM images, yielding an average thickness of 10.13 nm with a standard deviation of $\sigma = 1.02$ nm (10.1%) (Fig. S1). This result provides quantitative support for the observed core-shell morphology.

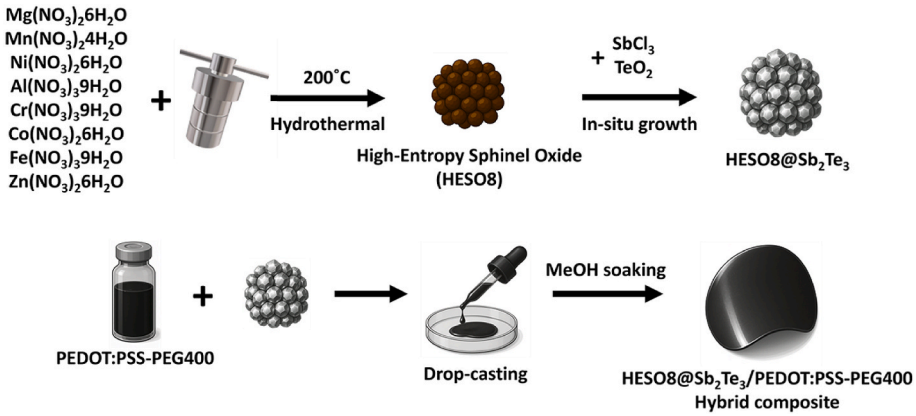


Fig. 1. Diagrammatic representation of the fabrication procedure for the composites.

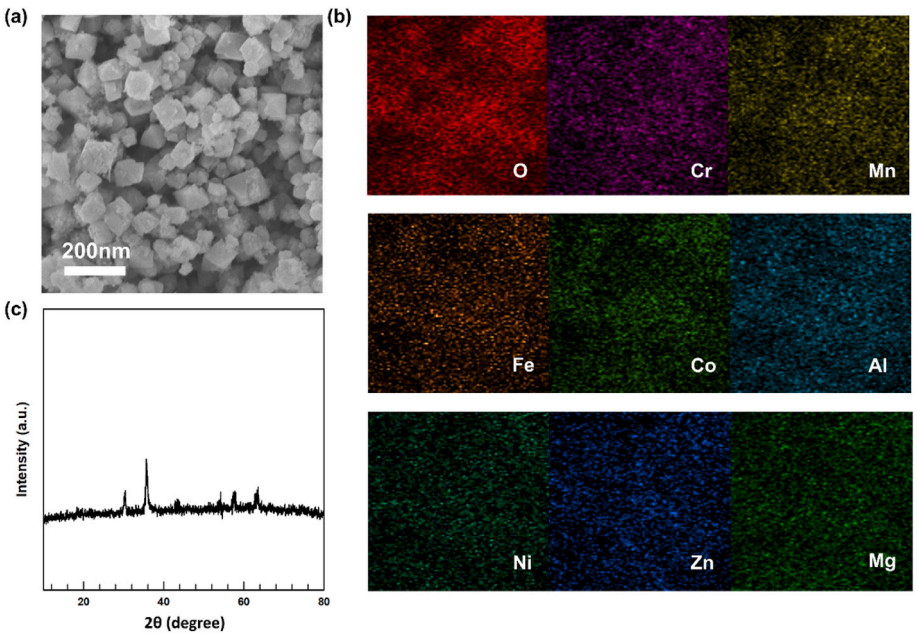


Fig. 2. (a) SEM image of High-Entropy Spinel Oxide8 (HESO8) particles, (b) EDS elemental mapping of HESO8 (Mg, Mn, Co, Ni, Zn, Al, Cr, Fe, O), (c) XRD pattern of HESO8.

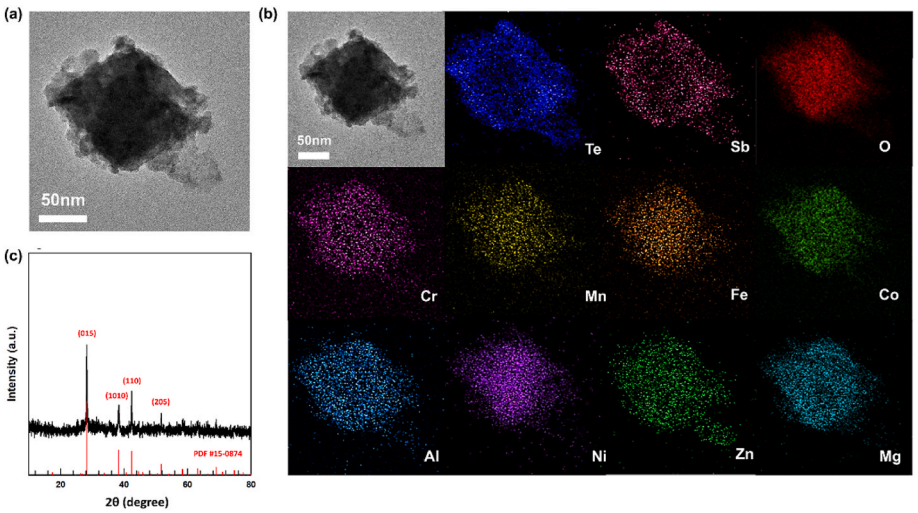


Fig. 3. (a) TEM image of HESO8@Sb_2Te_3 core–shell particles; (b) STEM–EDS elemental maps; (c) XRD pattern of HESO8@Sb_2Te_3.

2.3. Characterization of PEDOT:PSS-PEG matrix

Fig. 4 compares pristine PEDOT:PSS, a PEG-400–blended film, and the same blend after brief methanol immersion. In the FT-IR spectra (Fig. 4a), the neat PEDOT:PSS film exhibits only weak and broad features under our measurement conditions. Upon PEG-400 addition, distinct bands arising from both the host polymer and the plasticizer appear: a broad O–H stretching envelope at ~3200–3500 cm^{-1} attributable to hydrogen-bonded PEG within the sulfonated matrix, PEG C–H stretching modes in the 2950–2870 cm^{-1} region (with a clear component near 2875 cm^{-1}), and backbone-related C–S/C–O–C vibrations within 900–1200 cm^{-1}. The enhanced intensities at 2875 cm^{-1} (PEG C–H), 1645 cm^{-1} (C–O–H bending), and within the broad ~3300 cm^{-1} region confirm the incorporation and retention of PEG within the PEDOT:PSS matrix. After MeOH immersion, the PEG-related C–H stretching modes (2950–2870 cm^{-1}) and the broad O–H envelope around 3200–3500 cm^{-1} both decrease markedly in intensity, while the residual backbone bands become slightly sharper. These spectral changes indicate that a significant fraction of electrically insulating, weakly bound/free PEG-400 is removed from the film by the MeOH treatment and that the remaining polymer network undergAES a mild reorganization associated with secondary doping.

XPS S 2p spectra (Fig. 4b) further elucidate the evolution of the PEDOT:PSS–PEG matrix. The pristine PEDOT:PSS film (bottom spectrum) exhibits two well-resolved doublets, with a low-binding-energy pair at ~163.5–164.5 eV assigned to thiophene sulfur in PEDOT and a high-binding-energy pair at ~168.5–169.5 eV attributed to sulfonate sulfur in PSS. After PEG-400 blending (top spectrum), the overall S 2p intensity decreases and both the PEDOT- and PSS-related peaks appear substantially weaker than in the pristine film. In contrast, the MeOH-soaked PEDOT:PSS–PEG film (middle spectrum) recovers clearly resolved PEDOT- and PSS-derived doublets. Notably, the relative intensity of the high-binding-energy PSS-derived SO_3^- doublet is appreciably lower than in the pristine film, whereas the PEDOT thiophene

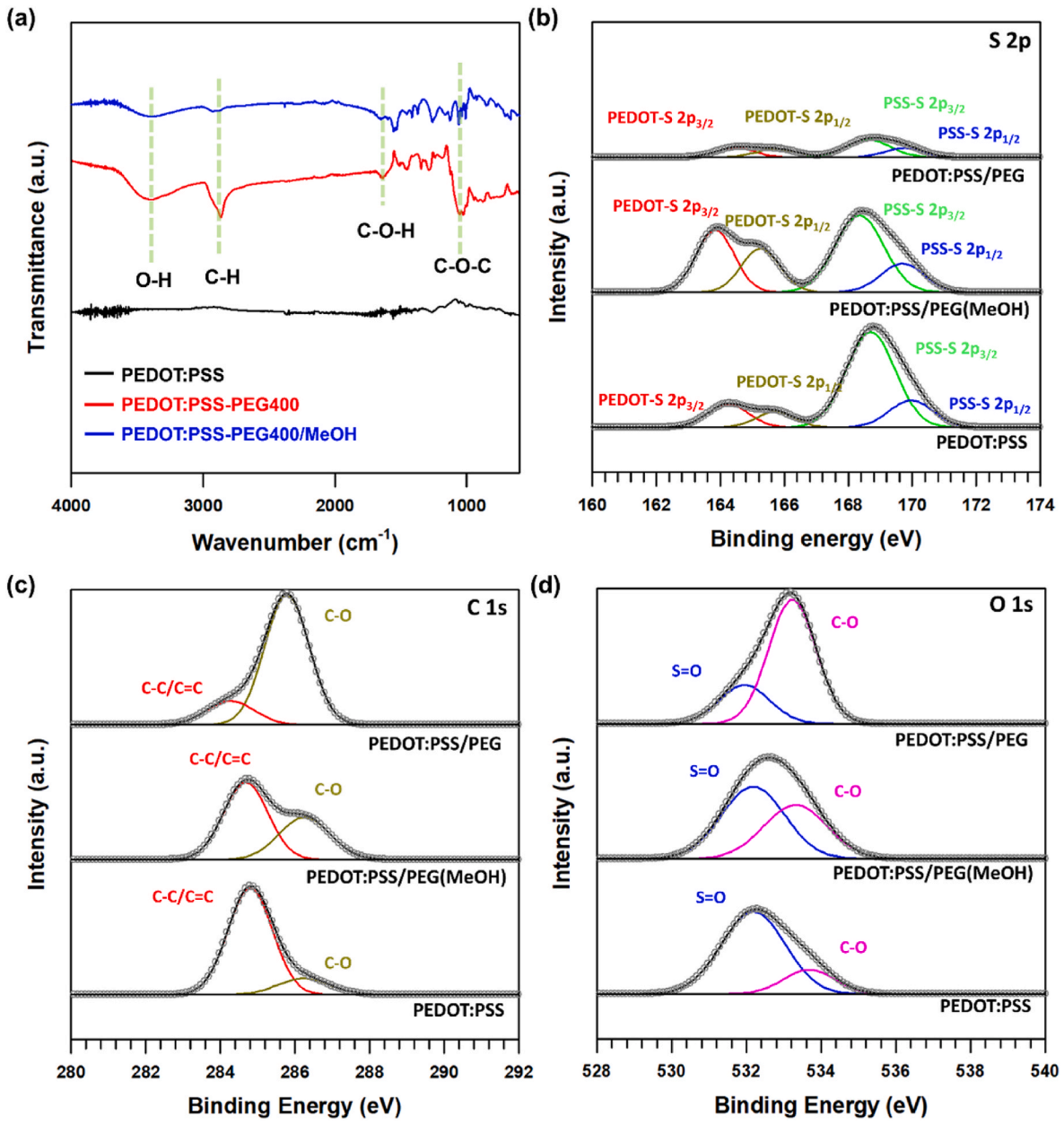


Fig. 4. (a) FT-IR spectra of PEDOT:PSS, PEDOT:PSS–PEG, and PEDOT:PSS–PEG (MeOH-soaked), (b) high-resolution XPS S 2p spectra of the same films, (c) high-resolution XPS C 1s spectra, (d) high-resolution XPS O 1s spectra.

contribution remains comparable. This systematic reduction of the PSS signal, without a corresponding loss of PEDOT-S, indicates that electrically insulating PSS together with *S*-free PEG-400 domains is selectively removed from the near-surface region during the MeOH treatment.

C 1s spectra (Fig. 4c) show that PEG-400 blending increases the relative contribution of the higher-binding-energy C–O/C–O–C components, leading to a more pronounced C–O character in the overall peak envelope. After MeOH soaking, this C–O-related contribution is reduced and the C 1s line shape reverts to a profile closely resembling that of pristine PEDOT:PSS. A similar trend is observed in the O 1s spectra (Fig. 4d): the PEDOT:PSS–PEG film exhibits an enhanced C–O/C–O–C contribution, which diminishes after MeOH treatment, yielding an O 1s peak distribution comparable to that of the neat PEDOT:PSS film. Taken together with the FT-IR and S 2p/P 2p results, these changes indicate that MeOH soaking partially removes PEG-400 and PSS from the near-surface region and reorganizes the matrix toward a more PEDOT-centered configuration.

Transport measurements (Fig. S2) exhibit a monotonic increase in room-temperature conductivity from ~8 S cm^{-1} for pristine PEDOT:PSS to ~15 S cm^{-1} for the PEG-400 blend and ~34 S cm^{-1} for the PEG-400 + MeOH film. The first enhancement is consistent with literature reports that PEG-induced charge screening between PEDOT and PSS promotes phase separation and rearrangement of PEDOT chains into larger, better-connected conducting domains, thereby improving interchain percolation [33]. The additional conductivity gain after MeOH soaking is ascribed to a secondary purification effect, in which electrically insulating PEG-400 and PSS are partially removed from the near-surface region, increasing the effective PEDOT volume fraction and connectivity. Overall, PEG reorganizes the intermolecular network and MeOH further refines the composition and morphology, yielding a PEDOT:PSS–PEG matrix with substantially enhanced conductivity while retaining sufficient solution processability for subsequent inorganic-filler integration.

2.4. Characterization of HESO8@Sb_2Te_3/PEDOT:PSS-PEG composite

Fig. 5a shows a bent HESO8@Sb_2Te_3/PEDOT:PSS composite film (inset: top-surface view), confirming that the disk-shaped specimen ($\phi \approx 22$ mm) remains self-supporting and flexible after incorporation of the core–shell filler. In cross-sectional FE-SEM images, neat PEDOT:PSS-PEG (Fig. 5b) exhibits a relatively continuous, feature-poor lamellar cross-section characteristic of a densely packed polymer film. By contrast, the 10 wt% HESO8@Sb_2Te_3/PEDOT:PSS-PEG composite (Fig. 5c) displays a more pronounced laminated microtexture with elongated interlamellar gaps, indicating that the core–shell particles are embedded within the PEDOT:PSS-PEG matrix while the overall layered integrity is retained. At a higher loading of 20 wt% (Fig. 5d), the cross-section becomes rougher and shows particle-rich protrusions and undulating layers, suggesting increased microstructural heterogeneity and partial aggregation of the inorganic domains. These observations imply that, at moderate filler levels (10 wt%), the core–shell particulates can be accommodated within the PEDOT:PSS-PEG framework without severe disruption, whereas higher loadings (20 wt%) introduce additional interfaces and defects that are expected to further enhance phonon scattering but may also begin to compromise the continuity of the electronic transport pathways.

2.5. Thermoelectric properties of HESO8@Sb_2Te_3/PEDOT:PSS-PEG composite

Temperature-dependent electrical conductivity (σ), Seebeck coefficient (S), and power factor (PF=S^2·σ) for composites with various filler loadings are summarized in Fig. 6a–c. In brief, σ reaches 89.5 S cm^{-1} at 425 K for the composition with 10 wt% filler. As seen in Fig. 6a, σ generally increases up to 375 K and then declines beyond 425 K. The high-temperature downturn arises from the combined effects of phonon–carrier scattering, the dominance of grain/defect-mediated scattering, and microstructural relaxation (grain coarsening, interface degradation, local lattice distortion), which shorten the carrier mean free path and reduce mobility [34,35].

Fig. 6b confirms p-type behavior with positive S across the measured range. Among the examined compositions, the 10 wt% sample exhibits the highest σ, whereas S increases with filler content and attains 201.03 μV K^{-1} at 475 K for 20 wt%.

To rationalize these trends, we invoke the standard transport relations:

$$\sigma = n\, e\, \mu \cdots \tag{3}$$

$$S = \frac{8\pi^2 {k_B}^2}{3eh^2} m^* T \left(\frac{\pi}{3n}\right)^{\frac{2}{3}} \cdots \tag{4}$$

where $n, e, \mu, k_B, h,$ and m^* denote the carrier concentration, elementary charge, mobility, Boltzmann constant, Planck constant, and effective mass, respectively [36]. Equations (3) and (4) directly explain the anticorrelation between S and n and the mobility penalty at high loadings: as filler content increases, enhanced interfacial scattering and possible particle agglomeration suppress μ, while chemical de-doping/trapping may reduce n [37,38]. Consequently, a trade-off emerges and σ peaks around 10 wt% (see Fig. 6c). The PF evolution (Fig. 6c) mirrors this balance, reaching 240.72 μW m^{-1} K^{-2} at 425 K for 10 wt%. To further substantiate the necessity of the Sb_2Te_3 shell, we compared these results with the electrical properties of composites

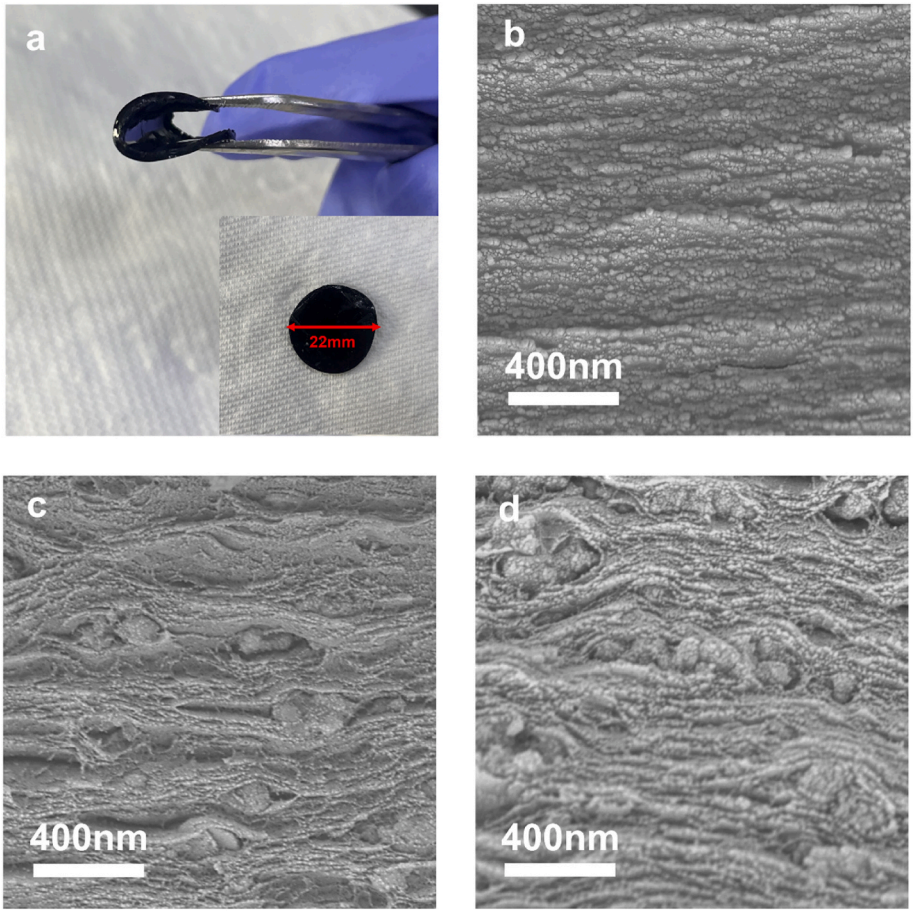


Fig. 5. (a) Digital photograph of the HESO8@Sb_2Te_3/PEDOT:PSS-PEG composite; inset: top-surface view. Cross-sectional FE-SEM images of (b) neat PEDOT:PSS-PEG,(c) 10 wt% HESO8@Sb_2Te_3/PEDOT:PSS-PEG and,(d) 20 wt% HESO8@Sb_2Te_3/PEDOT:PSS-PEG composite.

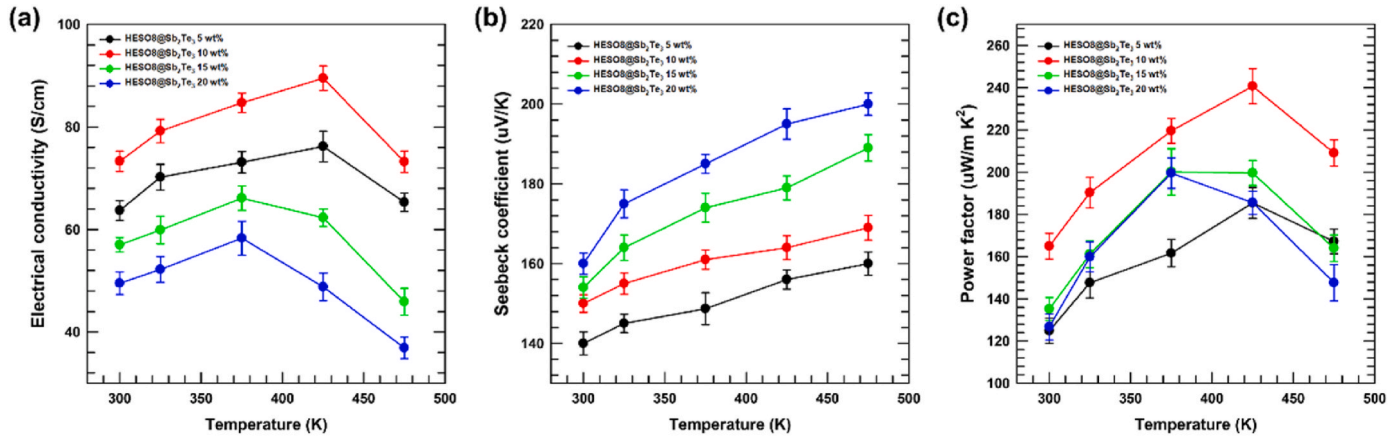


Fig. 6. Temperature-dependent thermoelectric properties of HESO8@Sb_2Te_3/PEDOT:PSS-PEG composites with 5, 10, 15, and 20 wt% filler: (a) electrical conductivity (four-probe), (b) Seebeck coefficient, (c) power factor (PF=$S^2\cdot\sigma$).

incorporating bare HESO8 fillers (Fig. S3). The HESO8-only composites exhibit extremely low electrical conductivity over the entire temperature range (Fig. S3a), which leads to severely limited power factors (Fig. S3c). These observations demonstrate that HESO8 alone cannot provide continuous electronic pathways, confirming that the Sb_2Te_3 shell is indispensable for sustaining σ and enabling meaningful PF enhancement. For comparison, the Sb_2Te_3-only composite exhibited slightly higher electrical conductivity and power factor than the HESO8@Sb_2Te_3 core-shell composite. (Fig. S4) This result indicates that Sb_2Te_3 primarily governs charge transport in the present system, while the role of the core-shell structure is not to maximize σ or PF alone, but to achieve a more balanced thermoelectric performance.

To further probe the carrier transport characteristics, temperature-dependent Hall measurements were carried out (Fig. S7). The Hall data show that the optimally loaded HESO8@Sb_2Te_3/PEDOT:PSS composite maintains relatively favorable mobility together with a moderated carrier concentration across the investigated temperature range. This trend indicates that the core-shell interfacial architecture influences carrier transport in a selective manner and provides additional support for a possible energy-filtering contribution. Moreover, although the carrier concentration generally increases with temperature, the carrier mobility decreases noticeably at higher temperature, particularly above 425 K. This behavior indicates that the conductivity degradation at elevated temperature is mainly associated with mobility loss rather than carrier depletion. Taken together, these results also help explain why 10 wt% is the optimal filler loading. At lower filler contents, the contribution of the HESO8@Sb_2Te_3 filler to interfacial transport modulation and thermal conductivity suppression is still limited. By contrast, at higher filler contents, the Hall results indicate a more pronounced mobility loss, which offsets the benefit of the increased Seebeck coefficient. Therefore, the 10 wt% composite provides the most favorable balance between electrical transport and thermal transport, resulting in the highest overall thermoelectric performance.

Total thermal conductivity (κ) is plotted in Fig. 7a and decreases with both temperature and filler fraction. To quantify this behavior, we decompose κ and evaluate the electronic contribution using the standard relations:.

$$\kappa = \kappa_e + \kappa_l \cdots \tag{5}$$

$$\kappa_e = L\,T\,\sigma \cdots \tag{6}$$

$$L = \left[1.5 + \exp\left(-\frac{|S|}{116}\right)\right] \times 10^{-8} \cdots \tag{7}$$

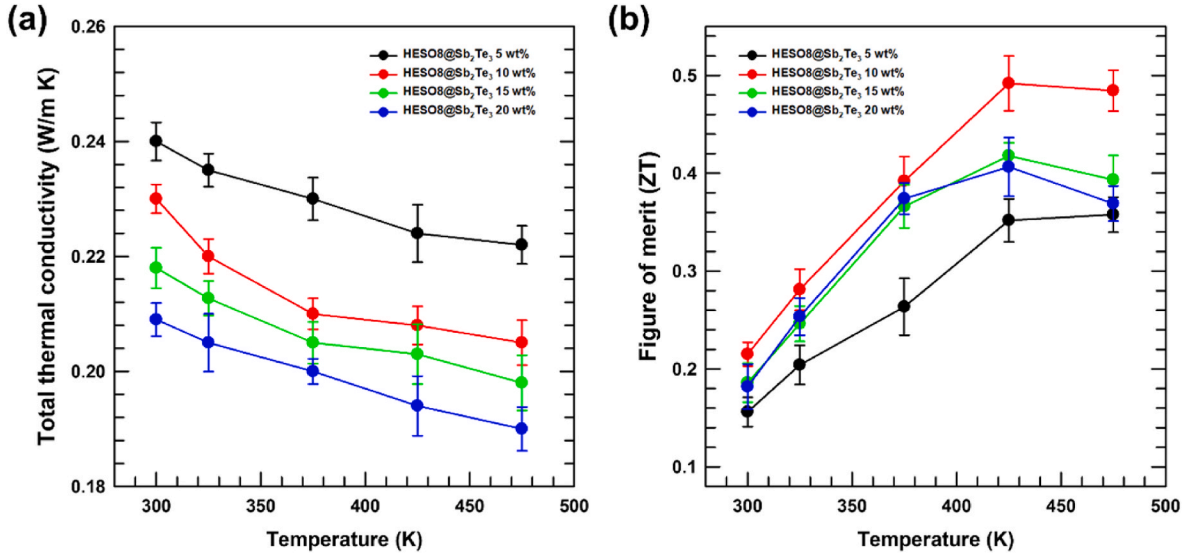


Fig. 7. Temperature-dependent thermophysical properties of HESO8@Sb_2Te_3/PEDOT:PSS-PEG composites with 5, 10, 15, and 20 wt% filler: (a) total thermal conductivity (LFA), (b) dimensionless figure of merit (ZT).

where κ_e and κ_L are the electronic and lattice thermal conductivities, L is the Lorenz number estimated from the measured S via Eq. (7), T is absolute temperature, and σ is the electrical conductivity. Using Eqs. (5)–(7), we obtained L, κ_e, and κ_L at 300 K (Table S2), confirming that lattice heat transport (κ_L) dominates in these composites [39,40]. To further examine the thermal role of the HESO8 core, its contribution was examined through comparison with HESO8-only composites, as shown in Fig. S5. The HESO8-only composites exhibit a pronounced decrease in total thermal conductivity, which is consistent with enhanced phonon scattering associated with mass/elastic disorder in the high-entropy oxide phase (Fig. S5a). However, because these composites suffer from extremely low σ (Fig. S3a), their resulting ZT values remain significantly limited (Fig. S5b). This comparison suggests that although HESO8 is effective in reducing κ, the shell component is essential for balancing electrical and thermal transport. In comparison with the Sb_2Te_3-only composite, the HESO8@Sb_2Te_3 core-shell composite showed lower thermal conductivity and slightly higher ZT, even though its electrical conductivity and power factor were somewhat lower (Fig. S6). This suggests that the core-shell configuration is more effective in improving the overall thermoelectric balance by suppressing thermal transport. Taken together, the results from Figs. S3 and S5 suggest that the Sb_2Te_3 shell serves as a key structural component for linking electrical transport with thermal conductivity reduction, supporting the usefulness of the core–shell strategy for flexible low-to mid-temperature thermoelectrics.

To assess the sensitivity of this analysis to the Lorenz-number model, additional calculations were also performed using $L = 1.5\times 10^{-8}$ and $L = 2.44 \times 10^{-8}$ W Ω K^{-2}, corresponding to the nondegenerate acoustic-scattering limit and the degenerate Sommerfeld limit, respectively (Tables S3 and S4). Although the absolute κ_e and κ_L values vary slightly depending on the assumed L, the electronic contribution remains minor and the conclusion that lattice heat transport dominates is unchanged. The observed reduction in κ_L is likely associated with the combined effects of (i) the high-entropy spinel (HESO8) core, which introduces chemical/mass disorder, elastic mismatch, and local strain fields; (ii) multiphase boundaries (core–shell–polymer), which increase thermal boundary resistance; and (iii) grain-boundary and shell-related nanostructural scattering in the Sb_2Te_3 shell. Together, these structural features suppress phonon transport, yielding a minimum κ of 0.19 W m^{-1} K^{-1} at 475 K for the 10 wt% composite. Consistent with the reduction in κ, the figure of merit ZT = $S^2\sigma T/\kappa$ (Fig. 7b) reaches 0.49 at 425 K for the 10 wt% composite. This improvement is attributed to the retained electronic transport through the continuous p-type Sb_2Te_3 shell network, together with reduced lattice heat transport promoted by the HESO8 core and the heterogeneous interfacial architecture. In combination with the optimized balance between S and σ, the composite exhibits a more favorable transport balance for mid-to low-temperature thermoelectric applications

To further clarify the significance of the present thermoelectric performance, the peak PF and ZT values of the 10 wt% HESO8@Sb_2Te_3/PEDOT:PSS-PEG composite were quantitatively compared with those of recently reported flexible thermoelectric composites, as summarized in Fig. S8. The present composite is positioned among the better-performing systems in the PF–ZT plot. Although its PF is not the highest among the compared flexible composites, it achieves a high ZT of 0.49 owing to its low thermal conductivity. This result indicates that the HESO8@Sb_2Te_3 core-shell architecture is effective in enhancing overall thermoelectric efficiency by reducing thermal conductivity while maintaining practical electrical transport.

2.6. Cycling stability of HESO8@Sb_2Te_3/PEDOT:PSS-PEG composite

To evaluate thermal stability near 150 °C, repeated thermal cycling tests were performed for the HESO8@Sb_2Te_3/PEDOT:PSS-PEG composite between room temperature and 150 °C. As shown in Fig. 8, the electrical conductivity gradually decreased after cycling, whereas the Seebeck coefficient remained relatively stable. Accordingly, the power factor showed a moderate decline, while retaining about 94.4% and 82.8% of its initial value after 5 and 10 cycles, respectively. This result indicates reasonable thermoelectric stability under repeated thermal cycling near 150 °C. Environmental stability is also an important consideration for PEDOT:PSS-based systems, since humidity, oxidation, and time-dependent resistance changes may affect long-term performance. Although these factors were not examined separately in the present study, they should be considered in future efforts toward practical device implementation. In addition to thermal cycling stability, the mechanical bending stability of HESO8@Sb_2Te_3/PEDOT:PSS, HESO8@Sb_2Te_3/PEDOT:PSS-PEG, and HESO8@Sb_2Te_3/PEDOT:PSS-PEG (MeOH) films was also evaluated. As shown in Fig. S9, the PEG-containing film exhibited the smallest resistance change during repeated bending at a fixed radius of 4 mm and under different bending radii, indicating improved mechanical flexibility and electrical stability. By contrast, the MeOH-treated film showed a relatively larger resistance variation, suggesting that the solvent treatment partially reduced the bendability of the film.

3. Conclusions

This work establishes a flexible thermoelectric platform by integrating high-entropy spinel oxide (HESO8) cores with Sb_2Te_3 shells in a PEDOT:PSS-PEG matrix, implementing a decoupled-transport architecture that preserves electronic conduction while selectively suppressing lattice heat flow. Disorder-driven phonon scattering from the HESO8

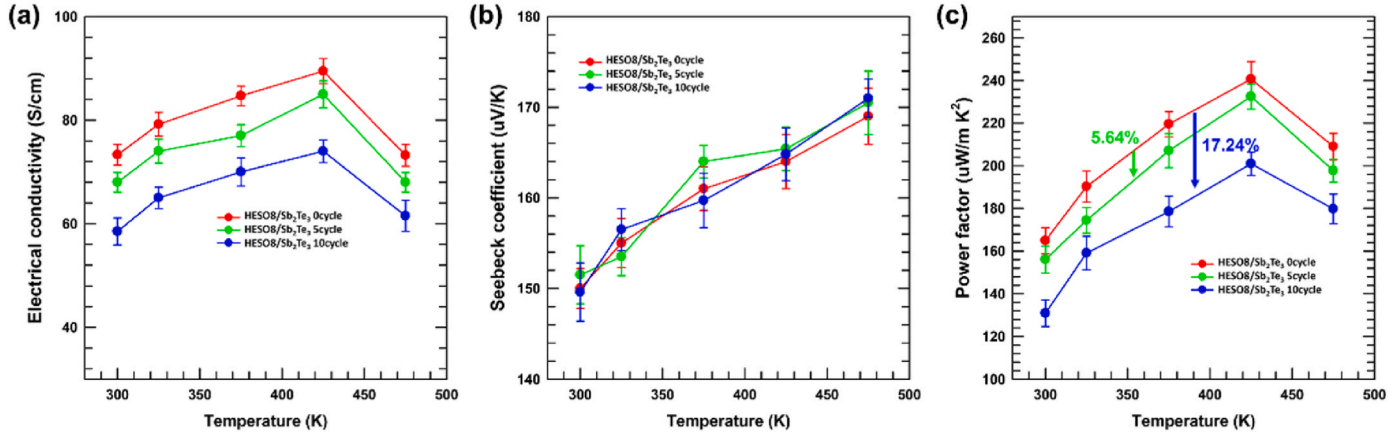


Fig. 8. Thermal cycling stability of the 10 wt% HESO8@Sb_2Te_3/PEDOT:PSS-PEG composite near 150 °C: (a) electrical conductivity, (b) Seebeck coefficient, and (c) power factor of the pristine sample and after 5 and 10 cycles.

core, together with the thermal boundary resistance at core–shell–polymer interfaces, effectively lowers the total thermal conductivity without compromising charge transport through the Sb_2Te_3 shell network. As a result, the composite achieves $\sigma = 89.5$ S cm^{-1}, $S = 164$ μV K^{-1}, PF = 240.7 μW m^{-1} K^{-2}, $\kappa = 0.21$ W m^{-1} K^{-1}, and ZT = 0.49 at 10 wt% and 425 K (Figs. 6 and 7, Table S1). The PEG/methanol-treated PEDOT:PSS matrix contributes to the formation of flexible, self-supporting composite films, while the added thermal cycling results indicate reasonable stability near 150 °C under repeated heating–cooling conditions. Collectively, these results demonstrate that the high-entropy core–shell design can deliver low κ alongside practical PF, yielding flexible composites with potential for low-to mid-temperature thermoelectric applications.

Declaration of competing interest

☒ The authors declare that they have no known competing financial interests or personal relationships that could have appeared to influence the work reported in this paper.

Acknowledgements

This work was supported by Korea Institute for Advancement of Technology (KIAT) grant funded by the Korea Government (MOTIE) (RS-2025-02263458, HRD Program for Industrial Innovation).supported by the National Research Foundation of Korea (NRF) grant funded by the Korea government(MSIT) (NRF-2022M3H4A1A02076956).

Appendix A. Supplementary data

Supplementary data to this article can be found online at https://doi.org/10.1016/j.jmrt.2026.04.128.

References

[1] Kwon O, Kim M, Kim J, Lee J, Lee S, Lee J, et al. Multistage pore structure in Bi2Te3/SiC composites: achieving lower thermal conductivity and enhanced thermoelectric performance. CrystEngComm 2025;27:5173–83. https://doi.org/10.1039/d5ce00519a.
[2] Kwon O, Kim M, Park D, Kim J. Enhanced thermoelectric performance of copper iodide particles/nanowires composite in the low-temperature range. Dalton Trans 2024;53:15305–15. https://doi.org/10.1039/d4dt02048k.
[3] Kwon O, Kim M, Lee J, Lee S, Kim J, Kim M, et al. High thermoelectric performance of Bi0.3Sb1.7Te3/PEDOT:PSS flexible composite via cation cross-linking. J Alloys Compd 2025;1014. https://doi.org/10.1016/j.jallcom.2025.178789.
[4] Hu B, Shi XL, Zou J, Chen ZG. Thermoelectrics for medical applications: progress, challenges, and perspectives. Chem Eng J 2022;437. https://doi.org/10.1016/j.cej.2022.135268.
[5] He J, Tritt TM. Advances in thermoelectric materials research: looking back and moving forward. Science 2017:357. https://doi.org/10.1126/science.aak9997. 1979.
[6] Zulkepli N, Yunas J, Mohamed MA, Hamzah AA. Review of thermoelectric generators at low operating temperatures: working principles and materials. Micromachines 2021;12. https://doi.org/10.3390/mi12070734. Basel.
[7] 7 n.d.
[8] Bell LE. Cooling, heating, generating power, and recovering waste heat with thermoelectric systems. n.d.
[9] Zebarjadi M, Esfarjani K, Dresselhaus MS, Ren ZF, Chen G. Perspectives on thermoelectrics: from fundamentals to device applications. Energy Environ Sci 2012;5:5147–62. https://doi.org/10.1039/c1ee02497c.
[10] Fu C, Sun Y, Felser C. Topological thermoelectrics. APL Mater 2020;8. https://doi.org/10.1063/5.0005481.
[11] Liu W, Hu J, Zhang S, Deng M, Han CG, Liu Y. New trends, strategies and opportunities in thermoelectric materials: a perspective. Mater Today Phys 2017;1:50–60. https://doi.org/10.1016/j.mtphys.2017.06.001.
[12] Li JF, Liu WS, Zhao LD, Zhou M. High-performance nanostructured thermoelectric materials. NPG Asia Mater 2010;2:152–8. https://doi.org/10.1038/asiamat.2010.138.
[13] Takabatake T, Suekuni K, Nakayama T, Kaneshita E. Phonon-glass electron-crystal thermoelectric clathrates: experiments and theory. Rev Mod Phys 2014;86:669–716. https://doi.org/10.1103/RevModPhys.86.669.
[14] Snyder GJ, Snyder AH. Figure of merit ZT of a thermoelectric device defined from materials properties. Energy Environ Sci 2017;10:2280–3. https://doi.org/10.1039/c7ee02007d.
[15] Duc C, Malliaras GG, Senez V, Vlandas A. Long-term ageing of PEDOT:PSS: wettability study. Synth Met 2018;238:14–21. https://doi.org/10.1016/j.synthmet.2018.02.003.
[16] Alam J, Xu X, Adu PCO, Meng Q, Zuber K, Afshar S, et al. Enhancing thermoelectric performance of PEDOT: PSS: a review of treatment and nanocomposite strategies. Advanced Nanocomposites 2024;1:16–38. https://doi.org/10.1016/j.adna.2023.08.001.
[17] Nassar NT, Brainard J, Gulley A, Manley R, Matos G, Lederer G, et al. Evaluating the mineral commodity supply risk of the U.S. manufacturing sector, vol. 6; 2020.
[18] Wei M, Zhong Y, Zhao G, Fan P, Ao D, Zheng Z, et al. Enhanced thermoelectric properties of Sb_2Te_3 thin films by in doping. Coatings 2023;13. https://doi.org/10.3390/coatings13101784.
[19] Yi G-C, Kim Y, Lee S, Lee E, Kim S, Suh W, et al. Molecular beam epitaxial step-edge growth of Bi2Te3/multi-stepped Sb_2Te_3 nanoplate hetero-structures. https://doi.org/10.21203/rs.3.rs-4586406/v1; 2024.
[20] Masoumi S, Zhussupbekov K, Prochukhan N, Morris MA, Pakdel A. A comprehensive investigation into thermoelectric properties of PEDOT:PSS/Bi0.5Sb1.5Te3 composites. J Mater Chem C Mater 2024;12:14314–29. https://doi.org/10.1039/d4tc00881b.
[21] Wang X, Wang H, Wu Y, Lian Y, Liu J, Zhao S. Water-assisted growth of Bi2Te3-Sb_2Te_3 lateral heterostructures for enhanced second harmonic generation. Chin J Chem Phys 2025;38:240–8. https://doi.org/10.1063/1674-0068/cjcp2401016.
[22] Chung KM, Adapa SR, Pei Y, Yeerella RH, Chen L, Shivakumar S, et al. Low thermal conductivity and diffusivity at high temperatures using stable high-entropy spinel oxide nanoparticles. Adv Mater 2025;37. https://doi.org/10.1002/adma.202406732.
[23] Tang Q, Jiang B, Wang K, Wang W, Jia B, Ding T, et al. High-entropy thermoelectric materials. Joule 2024;8:1641–66. https://doi.org/10.1016/j.joule.2024.04.012.
[24] Qiu G, Li T, Xu X, Liu Y, Niyogi M, Cariaga K, et al. High entropy powering green energy: hydrogen, batteries, electronics, and catalysis. NPJ Comput Mater 2025;11. https://doi.org/10.1038/s41524-025-01594-6.
[25] Yu B, Ren Y, Zeng Y, Ma W, Morita K, Zhan S, et al. Recent progress in high-entropy alloys: a focused review of preparation processes and properties. J Mater Res Technol 2024;29:2689–719. https://doi.org/10.1016/j.jmrt.2024.01.246.
[26] Oses C, Li T, Xu X, Han G, Qiu G, Owens JR. Beyond the four core effects: revisiting thermoelectrics with a high-entropy design. Mater Horiz 2025;12:5946–56. https://doi.org/10.1039/d5mh00356c.
[27] Zhang P, Gong L, Lou Z, Xu J, Cao S, Zhu J, et al. Reduced lattice thermal conductivity of perovskite-type high-entropy (Ca0.25Sr0.25Ba0.25RE0.25)TiO3 ceramics by phonon engineering for thermoelectric applications. J Alloys Compd 2022;898. https://doi.org/10.1016/j.jallcom.2021.162858.
[28] Mulla R, Dunnill CW. Core-shell nanostructures for better thermoelectrics. Mater Adv 2022;3:125–41. https://doi.org/10.1039/d1ma00955a.
[29] Li Y, Li X, Zhang S, Liu L, Hamad N, Bobbara SR, et al. Autonomic self-healing of PEDOT:PSS achieved via polyethylene glycol addition. Adv Funct Mater 2020;30. https://doi.org/10.1002/adfm.202002853.
[30] Oh JY, Shin M, Lee JB, Ahn JH, Baik HK, Jeong U. Effect of PEDOT nanofibril networks on the conductivity, flexibility, and coatability of PEDOT:PSS films. ACS Appl Mater Interfaces 2014;6:6954–61. https://doi.org/10.1021/am500769k. American Chemical Society.
[31] Biswas K, He J, Blum ID, Wu CI, Hogan TP, Seidman DN, et al. High-performance bulk thermoelectrics with all-scale hierarchical architectures. Nature 2012;489:414–8. https://doi.org/10.1038/nature11439.
[32] Aronov D, Andalman AS, Fee MS. A specialized forebrain circuit for vocal babbling in the juvenile songbird. Science 2008;320:630–4. https://doi.org/10.1126/science.1155140. 1979.
[33] Alemu Mengistie D, Wang PC, Chu CW. Effect of molecular weight of additives on the conductivity of PEDOT:PSS and efficiency for ITO-free organic solar cells. J Mater Chem A Mater 2013;1:9907–15. https://doi.org/10.1039/c3ta11726j.
[34] González-Hernández JE, Cubero-Sesin JM. Electrical conductivity of ultrafine-grained Cu and Al alloys: attaining the best compromise with mechanical properties. Mater Trans 2023;64:1754–68. https://doi.org/10.2320/matertrans.MT-MF2022046.
[35] Meng F, Ma J, He J, Li W. Phonon-limited carrier mobility and temperature-dependent scattering mechanism of 3C -SiC from first principles. Phys Rev B 2019;99. https://doi.org/10.1103/PhysRevB.99.045201.
[36] Kim M, Park D, Kim J. Thermoelectric performance of chalcogenide-free CaAl-layered double hydroxide–antimony trioxide nanowire composites with low thermal conductivity. Ceram Int 2024;50:3026–33. https://doi.org/10.1016/j.ceramint.2023.11.049.
[37] Patel SN, Glaudell AM, Peterson KA, Thomas EM, O'hara KA, Lim E, et al. Morphology controls the thermoelectric power factor of a doped semiconducting polymer. 2017.
[38] Huo B, Guo CY. Advances in thermoelectric composites consisting of conductive polymers and fillers with different architectures. Molecules 2022;27. https://doi.org/10.3390/molecules27206932.
[39] Kim HS, Gibbs ZM, Tang Y, Wang H, Snyder GJ. Characterization of Lorenz number with seebeck coefficient measurement. APL Mater 2015;3. https://doi.org/10.1063/1.4908244.
[40] Kim M, Park D, Kim J. Self-healing boron-doped Sb 2 Se 3 thermoelectric materials prepared using liquid metallic Ga-Sn alloys. n.d.